

Article

## Numerical Investigation of Two Double Swirl/Vortex Chamber Configurations for Turbine Blade Leading Edge Cooling

Pipat Tansakul<sup>1,3,a,b</sup>, Thanabodee Sinpo<sup>1,c</sup>, Phongsakorn Thawornsathit<sup>2,d</sup>,  
Varangrat Juntasaro<sup>2,e</sup>, and Ekachai Juntasaro<sup>1,f,\*</sup>

<sup>1</sup> Mechanical Engineering Simulation and Design Group, The Sirindhorn International Thai-German Graduate School of Engineering (TGGS), King Mongkut's University of Technology North Bangkok (KMUTNB), Bangkok 10800, Thailand

<sup>2</sup> Department of Mechanical Engineering, Faculty of Engineering, Kasetsart University, Bangkok 10900, Thailand

<sup>3</sup> Electricity Generating Authority of Thailand (EGAT), Nonthaburi 11130, Thailand

E-mail: <sup>a</sup>pipat.t-mesd2016@tggs.kmutnb.ac.th, <sup>b</sup>pipat.ta@egat.co.th,  
<sup>c</sup>thanabodee.s-mesd2017@tggs.kmutnb.ac.th, <sup>d</sup>phongsakorn.th@ku.th, <sup>e</sup>varangrat.j@ku.th,  
<sup>f</sup>\*ekachai.j@tggs.kmutnb.ac.th (Corresponding author)

**Abstract.** The objective of this work is to numerically assess the cooling performance of two double swirl/vortex chamber configurations (DSC and M-DVC). The predictive capability of five turbulence models is critically evaluated on fine and good-quality mesh for impinging and swirling flows. The averaged second norm  $L_2$  is employed to quantitatively measure the simulation error from each turbulence model compared to the experimental data. The RNG  $k - \varepsilon$  turbulence model with enhanced wall treatment is found to be the most accurate and suitable for the simulation of impinging and swirling flows. Various key physical and dimensionless parameters, including thermal performance factor, turbulence kinetic energy and vorticity, are used to comparatively assess the cooling performance of DSC and M-DVC under the laboratory testing condition and the real operating condition at base load. The results reveal that DSC can enhance better heat transfer due to higher turbulence kinetic energy. Also, much more uniform Nusselt number distribution is obtained by DSC owing to more symmetric and uniformly distributed velocity and vorticity. With the real operating condition, DSC even performs much better than M-DVC.

**Keywords:** Gas turbine, turbine blade cooling, leading edge, double swirl cooling, double vortex cooling.

ENGINEERING JOURNAL Volume 25 Issue 12

Received 13 July 2021

Accepted 19 December 2021

Published 30 December 2021

Online at <https://engj.org/>

DOI:10.4186/ej.2021.25.12.63

## 1. Introduction

Gas turbines are one of the most useful and reliable devices encountered in various applications such as power generation, oil and gas, process plants, as well as transportation. In the field of electric power generation, gas turbines are mainly used as mechanical drivers for both simple and combined cycle applications. To achieve the highest efficiency and support load flexibility to meet the demand of a modern grid, gas turbines are designed based on advanced technology for combustion systems and components which are concerned with minimization of leakages, advanced compressor aerodynamics, advanced performance of high-temperature combustion systems with low emission and management of cooling requirement. With these concepts, gas turbines operate at high turbine inlet temperature (TIT) above turbine metal temperature limit. To improve temperature-managing capability, high-temperature-resisting materials of turbine blades and vanes are integrated with complex cooling techniques such as internal cooling and external film cooling. These cooling techniques are used to prolong lifetime and operational requirement under extreme heat load conditions of gas turbines.

To design the most efficient turbine blade cooling system, it is necessary to consider cooling techniques that can generate suitable physical characteristics in considered parts. One of the most critical areas is the leading edge due to its function that directly confronts and absorbs the large amount of heat from hot gas. A large number of studies on mechanism and effect of cooling techniques on the turbine leading edge have been carried out. Comprehensive reviews have been reported by Han [2-4] and Town et al. [5]. Only some recent previous works are mentioned below. There are three main cooling techniques at the leading edge of gas turbine: (1) impingement cooling (IC), (2) vortex cooling (VC), or swirl cooling (SC), and (3) double vortex cooling (DVC), or double swirl cooling (DSC).

For impingement cooling, Taslim et al. [6] experimentally investigated the effects of different target wall roughness geometries on the convective heat transfer coefficient. The wall roughened with conical bumps proved to be the most effective geometry to obtain the highest heat transfer coefficient where the Nusselt number was increased up to 40% compared to that of the smooth wall. Taslim and Bethka [7] conducted both experimental and numerical studies to investigate the effect of crossflow on the heat transfer coefficient where the  $v_2f$  turbulence model was used for simulation with 1 million cells. The crossflow was found to reduce the heat transfer coefficient at the target wall. Elebiary and Taslim [8] confirmed that the crossflow produced by the upstream jet influenced the heat transfer coefficient due to its obstruction to the impingement flow to reach the target wall and also performed both experimental and numerical investigations to study the effects of flow arrangement and the number of nozzle holes on the Nusselt number of the target wall. The realizable  $k-\varepsilon$  turbulence model with

enhanced wall treatment was used for simulation with 1.1 million cells. The circular flow arrangement (flow from the coolant-chamber inlet and then reverse to the hub side of core chamber) with the number of 5 nozzle holes had the highest Nusselt number on the target wall. Yang et al. [9] experimentally and numerically investigated the spanwise-averaged Nusselt number distribution in the cooling passage of the leading edge where the Nusselt numbers obtained from measurements were compared with the correlation of Chupp et al. [10] with a maximum deviation of 6.5%. The numerical study was performed with the SST  $k-\omega$  turbulence model at steady (whole mesh), steady (half mesh) and unsteady (whole mesh) conditions using 5 million nodes. The best match between the numerical results and the experimental data was obtained by using the unsteady condition. The main factors that influenced the Nusselt number distribution on the target wall were (1) the target passage crossflow, (2) the Kelvin-Helmholtz vortex structure and (3) the unsteadiness associated with these phenomena. Unsteady oscillation of the impingement jets resulted in varying the stagnation locations. The Kelvin-Helmholtz vortex was the key factor that caused the impingement jets to oscillate. Wang et al. [11] experimentally and numerically investigated the effects of jet positions, i.e. center and tangential positions, on leading edge heat transfer by considering the averaged Nusselt number. There were two configurations: (1) semi-cylindrical core chamber with 10 cylindrical nozzles located along the axis (normal jet) of core chamber (representing the impingement chamber) and (2) semi-cylindrical core chamber with 10 cylindrical nozzles located along the edge (tangential jet) of core chamber (representing the vortex chamber). The realizable  $k-\varepsilon$  turbulence model was used for simulation with 2.5 million cells for the impingement chamber and 3.5 million cells for the vortex chamber. The averaged Nusselt numbers obtained by measurements were in excellent agreement with the correlation of Chupp et al. [10]. Both experimental and numerical results revealed that the local Nusselt number on the target wall increased with increasing jet Reynolds number. The tangential jets (vortex) provided more uniform Nusselt number distribution than the normal jets (impingement). The realizable  $k-\varepsilon$  turbulence model predicted the same trend of Nusselt number as the experimental data but the averaged Nusselt numbers on the target wall were under-predicted by 1%-10% depending on the jet Reynolds number.

For vortex or swirl cooling, Liu et al. [12] numerically investigated the effects of (1) Reynolds number (based on swirl chamber diameter), (2) the ratio of the swirl chamber radius to the jet slot height ( $R/d$ ) with a constant ratio of the swirl chamber radius to the jet nozzle length ( $R/b$ ) and (3) the ratio of the swirl chamber radius to the jet slot height with a constant jet nozzle area on the characteristics of flow (velocity, swirl number and pressure) and heat transfer (Nusselt number) where the swirl number was the ratio of the angular momentum flux to the linear

momentum flux of the swirl airstream. The SST  $k-\omega$  turbulence model was used for simulation with 2.08 million nodes. The global-area-weighted averaged Nusselt number of swirl chamber increased with increasing Reynolds number in any condition. With constant  $R/b$ , when  $R/d$  increased, the pressure loss increased and the swirl number also increased due to the increase in the circumferential velocity. Moreover, the Nusselt number based on swirl chamber diameter, the circumferentially averaged Nusselt number and the spanwise-averaged Nusselt number increased with increasing  $R/d$ . With constant jet nozzle area, there was no effect on swirl number when increasing  $R/d$  but the Nusselt number based on swirl chamber diameter, the circumferentially averaged Nusselt number and the spanwise-averaged Nusselt number decreased with increasing  $R/d$ . At higher  $R/d$  and higher Reynolds number, the cooling performance of swirl chamber was improved but the pressure loss was larger. Du et al. [13] numerically investigated the influence of nozzle geometry, i.e. the nozzle aspect ratio and the nozzle-to-chamber cross sectional area ratio, on flow and heat transfer performance where the standard  $k-\omega$  turbulence model was employed with 5.39 million cells. The averaged Nusselt number increased with increasing nozzle aspect ratio. The non-uniform Nusselt number distribution was captured at low nozzle-to-chamber cross sectional area ratio. Fan et al. [14] conducted both experimental and numerical studies on the effects of Reynolds number and the inlet-to-wall temperature ratio on heat transfer performance and flow behavior. The standard  $k-\omega$  turbulence model was employed for simulation with 7.95 million cells. The heat transfer coefficient was found to increase with increasing Reynolds number and with decreasing temperature ratio. In Wang et al. [15], the influences of the core chamber draft angle, the inlet-to-wall temperature ratio and the Reynolds number on flow (the pressure coefficient =  $(P - P_{out}) / (P_{int} - P_{out})$ ) and heat transfer (the Nusselt number, the thermal performance factor and the heat transfer capacity defined as  $Q = q_w A_w$  where  $q_w$  is the wall heat flux and  $A_w$  is the area of target wall) in variable cross-section vortex cooling were numerically studied. The standard  $k-\omega$  turbulence model was used for simulation with 4.04 million cells. With increasing core chamber draft angle, the spanwise-averaged Nusselt number increased while the pressure coefficient decreased. With increasing inlet-to-wall temperature ratio, the spanwise-averaged Nusselt number increased while the pressure coefficient decreased. The spanwise-averaged Nusselt number increased with increasing Reynolds number. Compared to the core chamber with uniform cross section, the core chamber with draft angle more than  $0^\circ$  gained more spanwise-averaged Nusselt number with lower pressure coefficient under the same Reynolds number and inlet-to-wall temperature ratio. Wang and

Han [16] conducted the experiment to study the effects of (1) the ratio of the leading-edge target-wall diameter to the nozzle diameter ( $D/d$ ), (2) the nozzle-to-nozzle spacing ( $s/d$ ) and (3) the jet Reynolds number on the area-averaged Nusselt number and the pressure loss coefficient defined as  $K = \Delta P / (\rho V^2 / 2)$ . The Nusselt number increased with increasing jet Reynolds number. Under the same jet Reynolds number, the nozzle configuration  $D/d = 4$  and  $s/d = 2$  provided the highest Nusselt number because more coolant was provided for smaller  $s/d$  and  $D/d = 4$  had the larger nozzle hole diameter. As the jet Reynolds number increased, the pressure loss coefficient increased. The pressure loss coefficient increased with increasing  $s/d$ .

For double vortex or swirl cooling, Lin et al. [17] performed the numerical study on alternative internal cooling configuration known as double swirl chambers cooling (DSC) in comparison with the impingement cooling. This study focused on the influences of three geometry parameters that affected cooling performance: (1) merging ratio, (2) nozzle inlet hole configuration and (3) radius of blunt protuberance. The Spalart-Allmaras turbulence model was employed with 3 million cells because its prediction was closest to the impingement-cooling experimental data of Yang et al. [18]. The computed Nu of DSC was found to be 24% higher than the Nu data of impingement cooling measured by Yang et al. [18] and the Nu distribution of DSC was more uniform. When merging ratio was higher, Nu decreased so that heat transfer was not effective but the pressure drop was reduced. Although the rectangular nozzle enhanced heat transfer better than the circular nozzle, its pressure drop was higher. Heat transfer was increased when using the rectangular nozzle with higher aspect ratio whose range of 1-3 was considered. The higher radius of blunt protuberance turned the heat transfer and pressure drop of DSC closer to those of the impingement cooling and the radius of blunt protuberance in the range of 0.5-1.0 was recommended. Zhou et al. [19] performed the comparative study of five DSC cases that had different length ratios of the vertical semi-axis to the horizontal semi-axis of the core chamber with the impingement cooling. The Spalart-Allmaras turbulence model was employed with 3 million cells because its prediction was closest to the experimental data of Wang et al. [11], Yang et al. [18], and Fecther et al. [20]. DSC experienced higher total pressure drop than impingement cooling. DSC with the largest length ratio of the vertical semi-axis to the horizontal semi-axis of core chamber had the lowest pressure drop and gained the highest spanwise-averaged Nusselt number and thermal performance factor whose values were higher than those of impingement cooling up to 27-30% and 29-33% respectively. The uniform heat transfer distribution was obtained at the target wall when the length ratio of the vertical semi-axis to the horizontal semi-axis of core chamber was reduced.

The effects of the merging ratio of core chambers and the aspect ratio of nozzles on cooling performance were numerically studied by Lin et al. [21] in case of double swirl chambers cooling. The computational setup was validated with the swirl-chamber experimental data of Hay and West [22] in terms of swirl flow number and Nusselt number ratio. The SST  $k-\omega$  turbulence model was employed with 2.89 million cells because its prediction was closest to the swirl-chamber experimental data of Hay and West [22]. The thermal performance factors of double swirl chambers (DSC) and swirl chamber (SC) were compared and found that the heat transfer performance of DSC was higher. When the merging ratio was higher, the Nusselt number ratio ( $Nu/Nu_0$ ) decreased so that heat transfer was not effective but the pressure drop was reduced. However, when the merging ratio was higher than 23%, the pressure drop was no longer affected. The *optimal* merging ratio for DSC was found to be in the range of 20-23% because the highest globally-averaged thermal performance factor was obtained in that range. The thermal performance factor was found to be maximum at the aspect ratio of 5. Comparative study was conducted by Fan et al. [23] to numerically investigate the heat transfer performance and pressure drop of five cooling configurations: two impingement cooling (IC with circular and rectangular nozzles), one vortex cooling (VC) and two double vortex cooling (M-DVC and T-DVC), whose volumes and hydraulic diameters of core chambers were equal for fair comparison on the same basis. The standard  $k-\omega$  turbulence model was employed with 1.825-2.862 million cells depending on the cooling configuration because its prediction was closest to the vortex-cooling experimental data of Fan et al. [14]. Among five cooling configurations, VC gained highest heat transfer performance with most uniformly distributed Nusselt number as indicated by the thermal performance factor but its pressure drop was also highest whereas M-DVC experienced lowest pressure drop.

It was clearly concluded by Lin et al. [17] and Zhou et al. [19] that the cooling performance of DSC was better than that of IC. However, when comparing the cooling performance of DSC with that of VC, it was unclear because Lin et al. [21] found DSC better than VC while Fan et al. [23] reported VC better than M-DVC. This inconsistent conclusion can be understood because the DSC core chamber of Lin et al. [21] and the M-DVC core chamber of Fan et al. [23] are different and tested at different conditions. Therefore, the present work is aimed to comparatively assess the cooling performance of DSC and M-DVC on the same basis by specifying that (1) the coolant chamber dimension, (2) the nozzle dimension and (3) the cross-sectional area and volume of the core chamber of both DSC and M-DVC must be equal. The *optimal* DSC configuration of Lin et al. [17] recently published is used to create the DSC dimension under the laboratory testing condition of Fan et al. [23]. Moreover, different turbulence models have been employed among different research groups. This work also attempts to

carefully select the most accurate turbulence model that can realistically predict both impingement and vortex because DSC involves partly impingement and partly vortex. The experimental data of Yang et al. [18] representing the impingement test case and Fan et al. [14] representing the vortex test case are used to evaluate the predictive capability of five turbulence models and also validate the computational setup. Those five turbulence models considered are the RNG  $k-\varepsilon$ , realizable  $k-\varepsilon$ , standard  $k-\omega$ , SST  $k-\omega$  and Spalart-Allmaras turbulence models. Very fine meshes with high mesh quality are used for simulation. The averaged second norm  $L_2$  is used to quantitatively measure the simulation error from each turbulence model compared to the experimental data. The circumferentially averaged Nusselt number, the totally averaged Nusselt number, the total pressure drop, the total pressure drop coefficient, the thermal performance factor, the velocity magnitude and streamline, the turbulence kinetic energy and its averaged magnitude over the cross section, the temperature, the vorticity and its averaged magnitude over the cross section are used to assess the cooling performance of DSC and M-DVC under the laboratory testing condition of Fan et al. [23] with the inlet Reynolds number of 18,500. Finally, both DSC and M-DVC are tested under the real operating condition of Electricity Generating Authority of Thailand (EGAT) at base load with the inlet Reynolds number of 40,000.

## 2. Computational details

### 2.1. Problem Description

Since the laboratory testing condition of Fan et al. [23] is selected for the cooling performance assessment of two double swirl/vortex chamber configurations at the turbine blade leading edge, the geometry and dimension of M-DVC according to Fan et al. [23] is shown in Fig. 1. In order to compare the cooling performance of DSC with that of M-DVC on the same basis, (1) the coolant chamber dimension, (2) the nozzle dimension and (3) the cross-sectional area and volume of the core chamber of both DSC and M-DVC must be equal so that the geometry and dimension of DSC is shown in Fig. 2 where the *optimal* DSC configuration of Lin et al. [17] in Table 1 is used to create the DSC dimension under the laboratory testing condition of Fan et al. [23].

Table 1. *Optimal* DSC configuration of Lin et al. [17].

Nozzle aspect ratio	5
Merging ratio (%)	25
Radius of blunt protuberance ( $r/D$ )	1

The definitions of three parameters in Table 1 are to be described. When the cross section of a nozzle is considered, the nozzle aspect ratio is the ratio of the



$$L_2(\phi) = \frac{\sqrt{\sum_{i=1}^N (\phi_i^{\text{sim}} - \phi_i^{\text{exp}})^2}}{N} \quad (2)$$

where the superscript *sim* denotes the simulation result, the superscript *exp* denotes the experiment data, the subscript *i* denotes the *i*th data point, and *N* is the number of data points. The variable of interest that will be used for the evaluation of the accuracy of five turbulence models is the circumferentially averaged Nusselt number, i.e.  $\phi = \text{Nu}_{ca}$ , and  $\text{Nu}_{ca}$  is defined as follows:

$$\begin{aligned} \text{Nu}_{ca} &= \frac{1}{N_{ca}} \sum_{i=1}^{N_{ca}} \left( \frac{h D_h}{\lambda} \right)_i = \frac{1}{N_{ca}} \sum_{i=1}^{N_{ca}} \left( \frac{q_w D_h}{(T_w - T_{in}) \lambda} \right)_i \\ &= \frac{1}{N_{ca}} \sum_{i=1}^{N_{ca}} \left( \frac{(T_w - T_1) D_h}{(T_w - T_{in}) (\Delta y)_i} \right)_i \end{aligned} \quad (3)$$

where *h* is the heat transfer coefficient,  $D_h$  is the hydraulic diameter of the cross section of the core chamber,  $\lambda$  is the thermal conductivity,  $q_w$  is the wall heat flux over the target wall,  $T_{in}$  is the inlet temperature of the cooling air,  $T_w$  is the target wall temperature,  $T_1$  is the temperature of the first cell center adjacent to the wall,  $(\Delta y)_i$  is the distance from the first cell center to the wall, and  $N_{ca}$  is the number of data points along the circumference.

Table 2. Numerical methods used.

Velocity-pressure coupling	SIMPLE
Gradient	Green-Gauss cell-based
Pressure	Second-order
Momentum	Second-order upwind
Turbulence models	Second-order upwind
Energy	Second-order upwind

All the simulations performed here are set up by using the numerical methods listed in Table 2. The flow condition is specified by the Reynolds number with the following definition:

$$\text{Re} = \frac{\rho V_{in} D_{h,coolant}}{\mu} \quad (4)$$

where  $\rho$  is the air density at the inlet of the coolant chamber,  $V_{in}$  is the averaged velocity over the inlet cross section of the coolant chamber calculated from the mass flow rate  $\dot{m} = \rho V_{in} A_{in}$  with  $A_{in}$  being the inlet cross-sectional area of the coolant chamber,  $D_{h,coolant}$  is the hydraulic diameter of the coolant chamber and  $\mu$  is the air dynamic viscosity at the inlet of the coolant chamber.

The boundary conditions of the Fan et al. [23] laboratory testing condition are provided in Table 3. The

boundary conditions of the EGAT real operating condition at base load are provided in Table 4.

Table 3. Boundary conditions of Fan et al. [23] laboratory testing condition.

Fan et al. [23]	
<b>Inlet condition</b>	
- Reynolds number	18,500
- Total temperature / K	350
<b>Target wall</b>	
- Temperature / K	500
<b>Outlet condition</b>	
- Pressure / Pa	160,000

Table 4. Boundary conditions of EGAT real operating condition at base load.

Real operating condition (EGAT)	
<b>Inlet condition</b>	
- Reynolds number	40,000
- Total pressure / Pa	748,801
- Total temperature / K	683
<b>Target wall</b>	
- Temperature / K	1,594
<b>Outlet condition</b>	
- Total pressure / Pa	677,757
- Total temperature / K	734

## 2.2. Data Reduction

The comparative evaluation of the cooling performance of both DSC and M-DVC is quantitatively assessed by using (1) the totally averaged Nusselt number ( $\text{Nu}$ ), (2) the total pressure drop ( $\Delta P_T$ ), (3) the total pressure drop coefficient ( $\eta$ ) and (4) the thermal performance factor (TPF). The totally averaged Nusselt number is numerically calculated over the whole target wall of the core chamber by averaging the circumferentially averaged Nusselt number as follows:

$$\text{Nu} = \frac{1}{N} \sum_{i=1}^N \text{Nu}_{ca,i} \quad (5)$$

where  $\text{Nu}_{ca}$  is the circumferentially averaged Nusselt number and *N* is the number of data points along the axial direction of the core chamber. The total pressure drop is expressed as:

$$\Delta P_T = P_{T,in} - P_{T,out} \quad (6)$$

where  $P_{T,in}$  is the total pressure at the inlet of the coolant chamber and  $P_{T,out}$  is the total pressure at the outlet of the core chamber. The total pressure drop coefficient is defined as:

$$\eta = \frac{\Delta P_T}{P_{T,in}} \quad (7)$$

which is the normalized total pressure drop. The thermal performance factor is defined as:

$$TPF = \frac{Nu / Nu_0}{(f / f_0)^{1/3}} \quad (8)$$

where  $Nu / Nu_0$  is the normalized Nusselt number,  $f / f_0$  is the normalized friction factor,  $Nu_0$  is the Nusselt number of fully developed turbulent flow through a smooth stationary pipe and  $f_0$  is the friction factor of fully developed turbulent flow through a smooth stationary pipe. In this work, the correlations of Kays and Crawford [1] are adopted for  $Nu_0$  and  $f_0$  with the following formulations:

$$Nu_0 = 0.022 Re^{0.8} Pr^{0.5} \quad (9)$$

$$f_0 = 0.184 Re^{-0.2} \quad (10)$$

where  $Re$  is the Reynolds number whose definition is given in Eq. (4) and  $Pr$  is the Prandtl number whose values for air are  $Pr = 0.71$  in the test case of Fan et al. [23] laboratory testing condition and  $Pr = 0.65$  in the test case of EGAT real operating condition at base load in this work. The friction factor is formulated as:

$$f = \frac{\Delta P_T}{\left(\frac{1}{2} \rho V_{in}^2\right) \left(\frac{L_f}{D_{h,core}}\right)} \quad (11)$$

where  $L_f$  is the streamwise distance from the coolant chamber inlet to the core chamber outlet through one nozzle whose values are  $L_f = 127.3$  mm for DSC and  $L_f = 128$  mm for M-DVC, and  $D_{h,core}$  is the hydraulic diameter of the core chamber.

### 3. Validation of Computational Setup

#### 3.1. Validation Test Case 1: Yang et al. [18]

The test case of Yang et al. [18] is used to select the most accurate turbulence model that can capture physics of the impinging flow. The geometry and dimension of this test case is illustrated in Fig. 5. Figure 6 displays the mesh distribution used with the number of 9.82-million cells. Boundary conditions are summarized in Table 5.

Figure 7 shows the distribution of the circumferentially averaged Nusselt number ( $Nu_{ca}$ ) along the target wall of the core chamber in the axial direction in which the centers of 10 nozzles are marked and the simulation results of 5 turbulence models are compared with the experimental data of Yang et al. [18]. From the experimental data, the peak of  $Nu_{ca}$  is convected downstream of its nozzle due to crossflow along the core chamber from the nozzle no.1 to the outlet. The

maximum  $Nu_{ca}$  is induced by the nozzle no.3 and there are 2 peaks. Elsewhere,  $Nu_{ca}$  has only one peak.

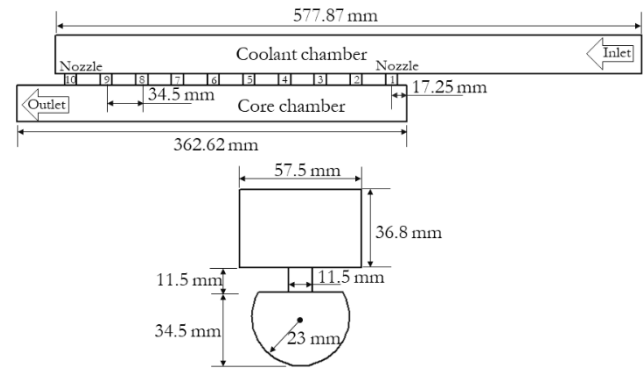


Fig. 5. Geometry and dimension of test case Yang et al. [18].

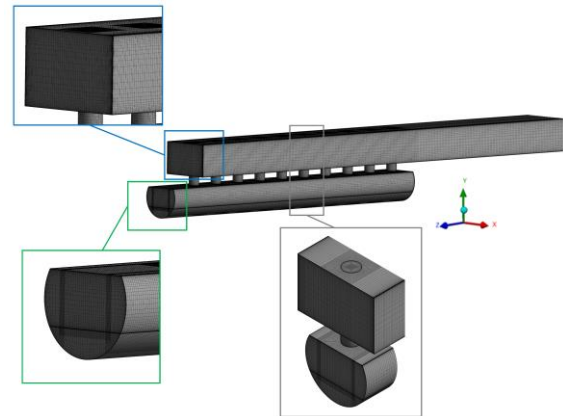


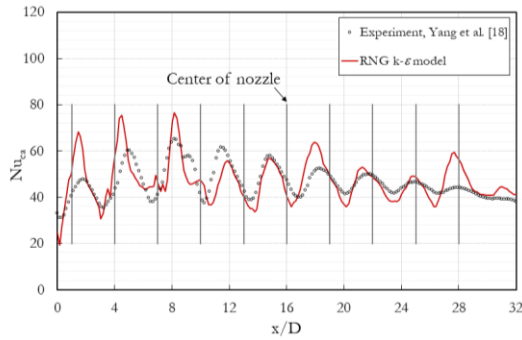
Fig. 6. Mesh of test case Yang et al. [18].

Table 5. Boundary conditions of test case Yang et al. [18].

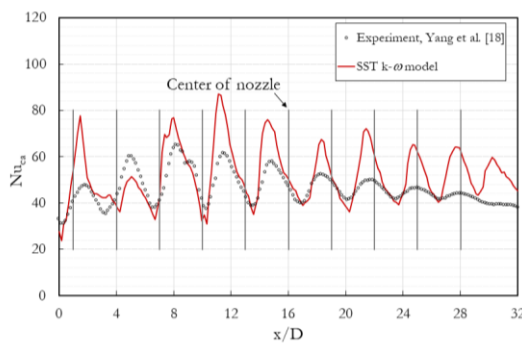
Yang et al. [18]	
<b>Inlet condition</b>	
- Reynolds number	15,000
- Temperature / K	348.15
<b>Target wall</b>	
- Temperature / K	419.15
<b>Outlet condition</b>	
- Pressure / Pa	101,325

The  $Nu_{ca}$  peak increases from the nozzle no.1 to no.3 and then decreases from the nozzle no.3 to no.9 and without peak for the nozzle no.10. Since there is no discernable difference among the simulation results obtained from 5 turbulence models, the averaged second norm is adopted here as an indicator to identify which turbulence model can predict  $Nu_{ca}$  most accurately. The averaged second norms of 5 turbulence models are determined as reported in Table 6 where the RNG  $k - \epsilon$  turbulence model with enhanced wall treatment is found

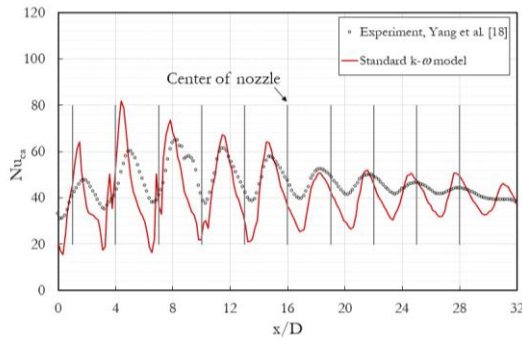
to be the most accurate one because its averaged second norm is lowest, compared to those of other turbulence models, so that it is suitable for the impinging flow simulation.



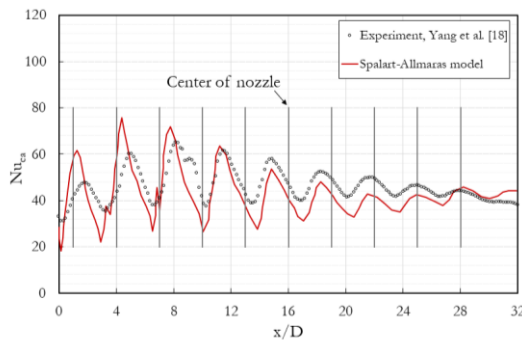
(a) RNG  $k-\epsilon$  model.



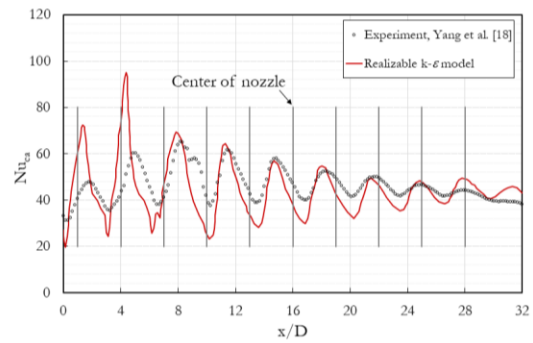
(b) SST  $k-\omega$  model.



(c) Standard  $k-\omega$  model.



(d) Spalart-Allmaras model.



(e) Realizable  $k-\epsilon$  model.

Fig. 7. Distribution of circumferentially averaged Nusselt number along the target wall of the core chamber in the axial direction of test case Yang et al. [18]: (a) RNG  $k-\epsilon$  model, (b) SST  $k-\omega$  model, (c) Standard  $k-\omega$  model, (d) Spalart-Allmaras model, and (e) Realizable  $k-\epsilon$  model.

Table 6. Averaged second norms of test case Yang et al. [18].

Turbulence model	Second norm (avg)
RNG $k-\epsilon$	0.72
SST $k-\omega$	0.78
Standard $k-\omega$	0.82
Spalart-Allmaras	0.91
Realizable $k-\epsilon$	1.07

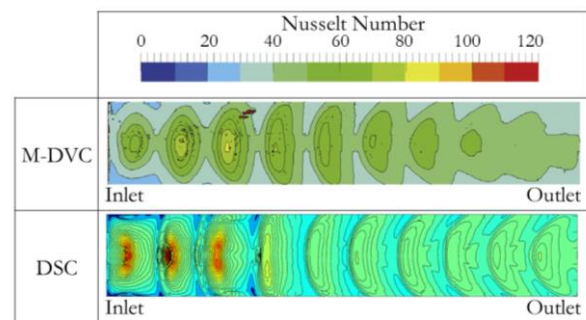


Fig. 8. Contour of the Nusselt number over the target wall of test case Yang et al. [18].

In Fig. 8, the contour of the Nusselt number is displayed over the target wall that covers the curved surface from  $-75^\circ$  to  $+75^\circ$  degree and the stagnation line is located at  $0^\circ$ . For this contour plot, the curved surface is unfolded into a plane surface. The predicted contour is in reasonable agreement with the measured contour where the top-3 regions of high Nusselt number are detected at the nozzle no. 2, 3 and 4 by the measurement and at the nozzle no. 1, 2 and 3 by the

simulation. However, the magnitude of the predicted Nusselt number is higher than that of the measured one.

### 3.2. Validation Test Case 2: Fan et al. [14]

The test case of Fan et al. [14] is used to select the most accurate turbulence model that can capture physics of the swirling/vortex flow. The geometry and dimension of this test case is illustrated in Fig. 9. Figure 10 displays the mesh distribution used with the number of 9.75-million cells. Boundary conditions are summarized in Table 7.

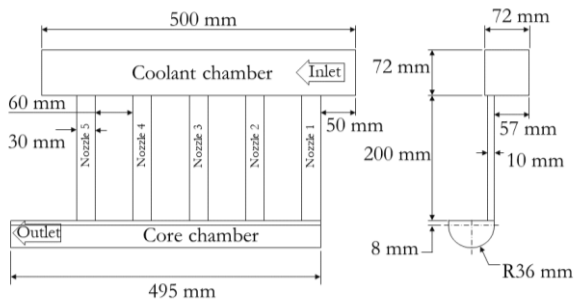


Fig. 9 Geometry and dimension of test case Fan et al. [14].

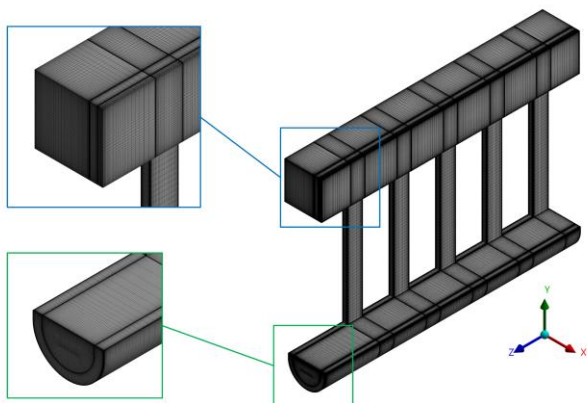
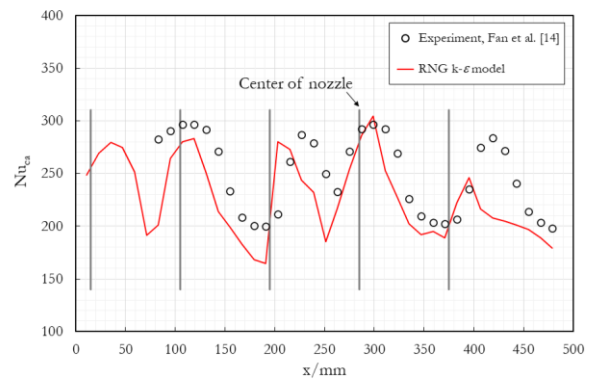


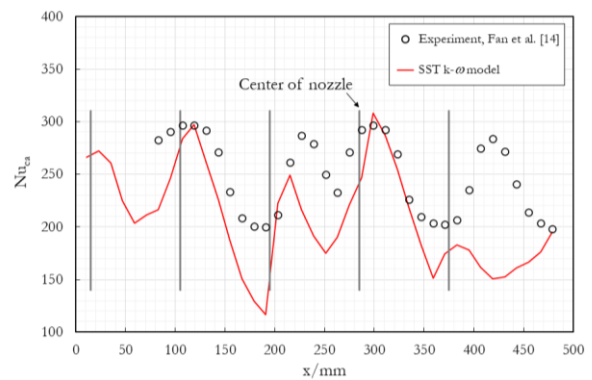
Fig. 10 Mesh of test case Fan et al. [14].

Table 7. Boundary conditions of test case Fan et al. [14].

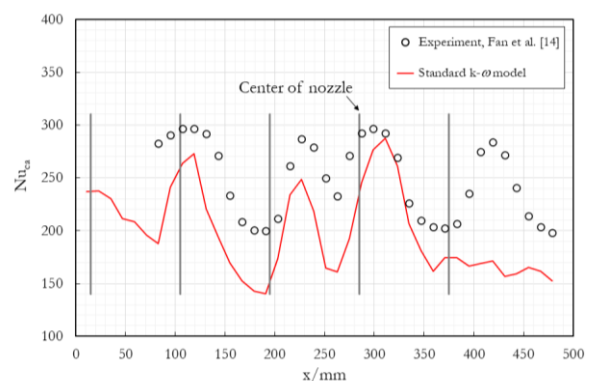
Fan et al. [14]	
<b>Inlet condition</b>	
- Reynolds number	28,537
- Temperature / K	288
<b>Target wall</b>	
- Temperature / K	327.27
<b>Outlet condition</b>	
- Pressure / Pa	101,325



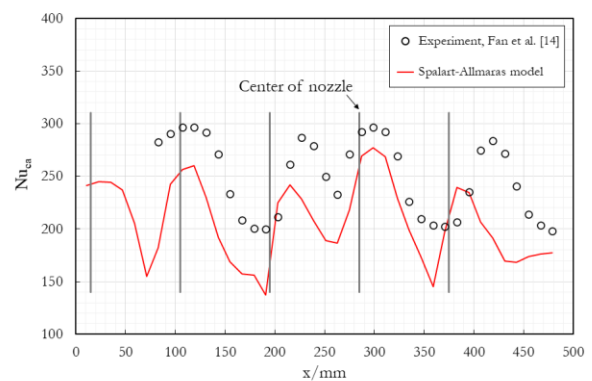
(a) RNG  $k-\epsilon$  model.



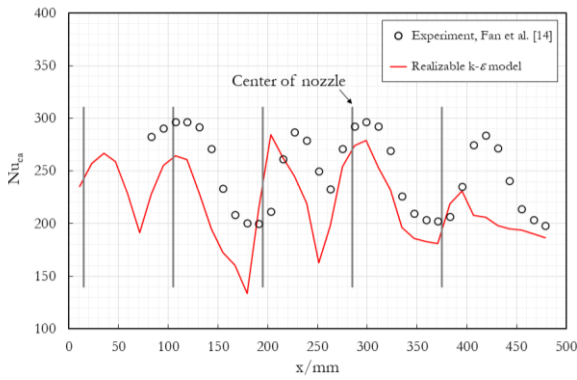
(b) SST  $k-\omega$  model.



(c) Standard  $k-\omega$  model.



(d) Spalart-Allmaras model.



(e) Realizable  $k-\epsilon$  model.

Fig. 11. Distribution of circumferentially averaged Nusselt number along the target wall of the core chamber in the axial direction of test case Fan et al. [14]: (a) RNG  $k-\epsilon$  model, (b) SST  $k-\omega$  model, (c) Standard  $k-\omega$  model, (d) Spalart-Allmaras model, and (e) Realizable  $k-\epsilon$  model.

Figure 11 shows the distribution of the circumferentially averaged Nusselt number ( $Nu_{ca}$ ) along the target wall of the core chamber in the axial direction in which the centers of 5 nozzles are marked and the simulation results of 5 turbulence models are compared with the experimental data of Fan et al. [14] where no experimental data was given around the nozzle no.1. From the experimental data, the peak of  $Nu_{ca}$  is convected downstream of its nozzle due to crossflow along the core chamber from the nozzle no.2 to the outlet, similar to the test case of Yang et al. [18]. The maximum  $Nu_{ca}$  is induced by the nozzle no.2 and no.4. All nozzles considered have only one  $Nu_{ca}$  peak. The  $Nu_{ca}$  peaks seem to be not much different among themselves, the uniformity of which is enhanced by the swirling/vortex flow to evenly promote the convective heat transfer rate.

Table 8. Averaged second norms of test case Fan et al. [14].

Turbulence model	Second norm (avg)
RNG $k-\epsilon$	6.67
Realizable $k-\epsilon$	7.85
Spalart-Allmaras	9.16
SST $k-\omega$	9.94
Standard $k-\omega$	10.44

Since there is barely perceptible difference among the simulation results obtained from 5 turbulence models, the averaged second norm is used again to quantitatively measure the difference between each simulation result and the experimental data. The lowest averaged second norm indicates the most accurate turbulence model that can predict this  $Nu_{ca}$  distribution. The averaged second

norms of 5 turbulence models are given in Table 8 where the RNG  $k-\epsilon$  turbulence model with enhanced wall treatment is found to be the most accurate one again so that it is suitable for the swirling/vortex flow simulation.

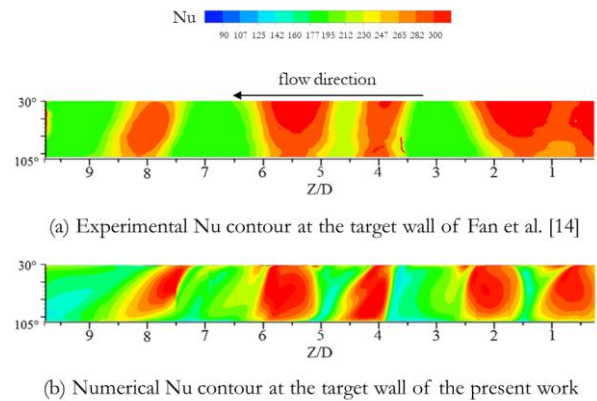


Fig. 12. Contour of the Nusselt number over the target wall: (a) Experimental data of Fan et al. [14], and (b) Numerical result of the present work.

Figure 12 shows the contour of the Nusselt number ( $Nu$ ) over the target wall from  $30^\circ$  to  $105^\circ$  along the curved surface in which the contour of the Nusselt number obtained from the RNG  $k-\epsilon$  turbulence model with enhanced wall treatment is compared to that of the experimental data of Fan et al. [14]. It reveals that the RNG  $k-\epsilon$  contour is in good agreement with the experimental data of Fan et al. [14].

#### 4. Results and Discussion

The main focus of the present investigation is to comparatively assess the cooling performance of DSC and M-DVC under (1) the laboratory testing condition of Fan et al. [23], and (2) the EGAT real operating condition at base load. The results of the current study are presented in the following 2 subsections: (1) the comparative evaluation of DSC and M-DVC under the laboratory testing condition of Fan et al. [23] and (2) the comparative evaluation of DSC and M-DVC under the EGAT real operating condition at base load.

##### 4.1. Comparative Evaluation of DSC and M-DVC under Laboratory Testing Condition of Fan et al. [23]

The laboratory testing condition of Fan et al. [23] is conducted at  $Re = 18,500$ . In order to compare the circumferentially averaged Nusselt number ( $Nu_{ca}$ ) between DSC and M-DVC on the same basis, the curved length of the circumference ( $L_{ca}$ ) used to calculate  $Nu_{ca}$  should be equal between DSC and M-DVC which is  $L_{ca} = 26.32$  mm in this work as shown in Fig. 13.

Figure 14 shows the distribution of circumferentially averaged Nusselt number along the target wall in the axial

direction under the laboratory testing condition of Fan et al. [23] where the simulation result of DSC is compared to the M-DVC one. It is found that all  $Nu_{ca}$  peaks of DSC are higher than the M-DVC ones and the totally averaged Nusselt number of DSC is larger up to 52.64% compared to that of M-DVC as given in Table 9. The  $Nu_{ca}$  peaks of DSC are quite uniform while the M-DVC ones are not with a reduced peak at the nozzle no.4. It is quite obvious that the  $Nu_{ca}$  of DSC has two separate peaks at each nozzle whereas the  $Nu_{ca}$  of M-DVC apparently has only one peak. There seems to be a valley between two  $Nu_{ca}$  peaks of each DSC nozzle and the valley is approximately located at the center of each nozzle. The  $Nu_{ca}$  peaks of M-DVC are located a little downstream of the center of each nozzle, except for the last nozzle where the  $Nu_{ca}$  peak is located a little upstream of the nozzle center.

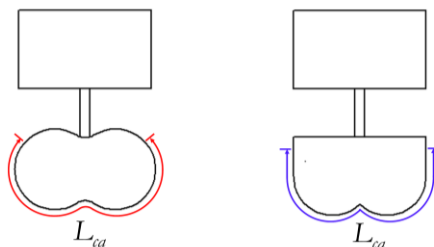


Fig. 13. Same curved length of the circumference ( $L_{ca}$ ) for calculating circumferentially averaged Nusselt numbers of DSC (left) and M-DVC (right).

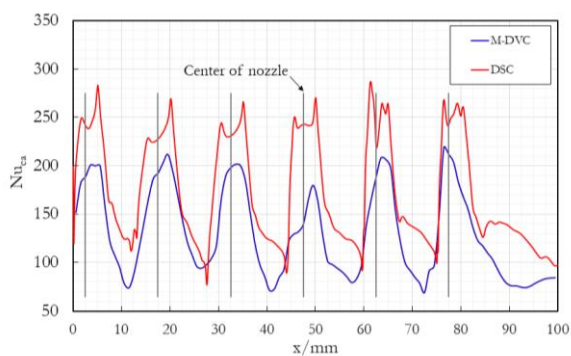


Fig. 14. Circumferentially averaged Nusselt number along the target wall in the axial direction under the laboratory testing condition of Fan et al. [23].

Figure 15 illustrates the Nusselt number contours of M-DVC and DSC on the target wall using the laboratory testing condition of Fan et al. [23]. It is found that the Nusselt number distribution of DSC is more symmetric to the symmetric line than that of M-DVC. From this contour plot, it is quite clear that there are two separate regions of high Nusselt number at each nozzle of DSC while there is only one high Nusselt number region at each nozzle in case of M-DVC. The nozzle no.4 of M-DVC

cannot have the impinging jet on the target wall so that its  $Nu_{ca}$  is lower than other nozzles.

In Table 9, the simulation results of the totally averaged Nusselt number, the total pressure drop, the total pressure drop coefficient and the thermal performance factor using the laboratory testing condition of Fan et al. [23] are summarized in case of DSC and M-DVC. The totally averaged Nusselt number ( $Nu$ ) of DSC is higher than that of M-DVC by 52.64%; in other words, DSC can enhance better heat transfer than M-DVC. Moreover, the total pressure drop ( $\Delta P_T$ ) of DSC is also higher than that of M-DVC by 18.85%, which implies that more friction is encountered in DSC compared to M-DVC. However, when the total pressure drop is normalized by the total pressure at inlet to obtain the total pressure drop coefficient ( $\eta$ ), DSC is more efficient than M-DVC to overcome friction because the  $\eta$  of DSC is less than that of M-DVC by 10.87%. This finding is confirmed by the thermal performance factor (TPF) where DSC gains higher TPF than M-DVC by 38.10%.

Table 9. Totally averaged Nusselt number, total pressure drop, total pressure drop coefficient and thermal performance factor in case of the laboratory testing condition of Fan et al. [23].

Parameter	M-DVC	DSC	Difference (%)
Totally averaged Nusselt number	130.42	199.07	+52.64
Total pressure drop, Pa	16,830.54	20,002.76	+18.85
Total pressure drop coefficient	0.92	0.82	-10.87
Thermal performance factor	0.63	0.87	+38.10

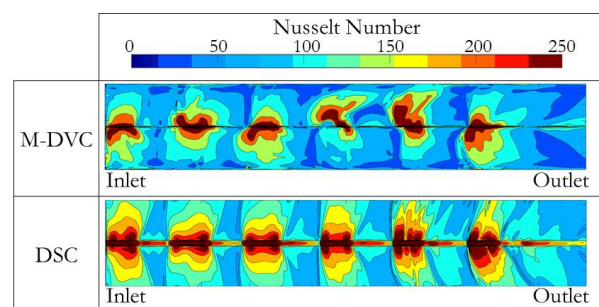


Fig. 15. Nusselt number contours of M-DVC and DSC on the target wall using the laboratory testing condition of Fan et al. [23].

Figure 16 shows the velocity magnitude contours and streamlines of M-DVC and DSC over the XY cross section through the middle plane of each individual nozzle under the laboratory testing condition of Fan et al. [23]. It

is found that the impinging jets of DSC from six nozzles generate the stagnation points at the expecting area as designed which is in the middle between two core chambers merging to form the target wall opposite to the nozzle exit. For M-DVC, the impinging jet of the nozzle no.4 misses the target wall and the consequence can be noticed in Fig. 14 and 15 where its  $Nu_{ca}$  peak is lower than those of other nozzles and its high Nusselt number region is not on the target wall, meaning lower cooling performance. It also reveals that two counter-rotating vortices formed by DSC are more symmetric for each nozzle and more uniform among six nozzles than those of M-DVC.

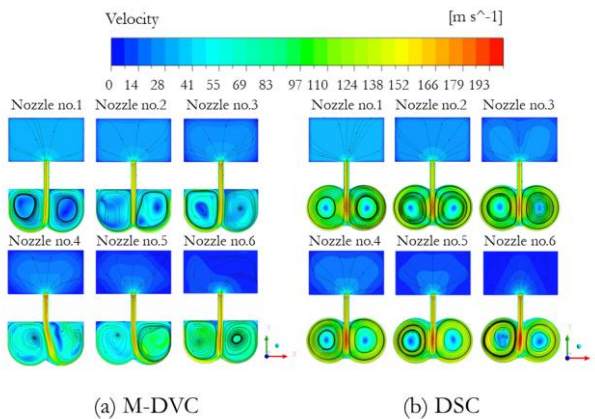


Fig. 16. Velocity magnitude contour and streamline over the XY cross section through the middle plane of each individual nozzle under the laboratory testing condition of Fan et al. [23]: (a) M-DVC and (b) DSC.

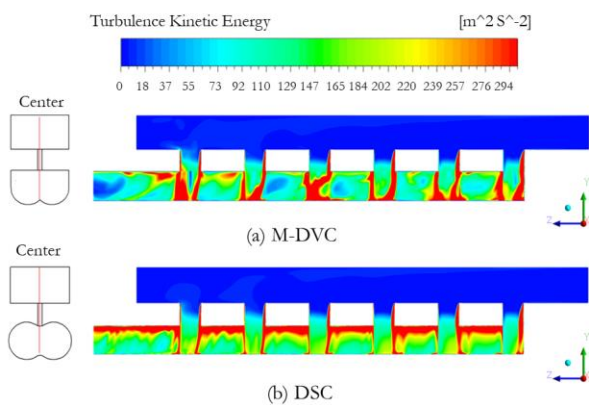


Fig. 17. Turbulence kinetic energy contour over the YZ cross section at the middle plane through six nozzles under the laboratory testing condition of Fan et al. [23]: (a) M-DVC and (b) DSC.

Figure 17 displays the turbulence kinetic energy ( $k$ ) contours of M-DVC and DSC over the YZ cross section at the middle plane through six nozzles under the laboratory testing condition of Fan et al. [23]. It is found that the averaged magnitude of  $k$  over the whole YZ cross section of the core chamber of DSC ( $k_{avg} = 209.64 \text{ m}^2/\text{s}^2$ )

is higher than that of M-DVC ( $k_{avg} = 184.02 \text{ m}^2/\text{s}^2$ ) so that DSC can generate more turbulence to enhance heat transfer. At the nozzle no.4 of M-DVC, the high- $k$  zone seems not to be pushed down enough toward the target wall so that its  $Nu_{ca}$  peak is lower than those of other nozzles.

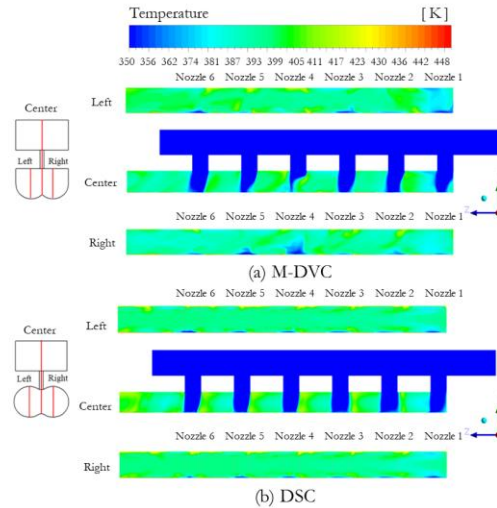


Fig. 18. Temperature contour over the YZ cross section at the middle plane of left and right core chambers and at the middle plane through six nozzles under the laboratory testing condition of Fan et al. [23]: (a) M-DVC and (b) DSC.

Figure 18 illustrates the temperature contours of M-DVC and DSC over the YZ cross section at the middle plane of left and right core chambers and at the middle plane through six nozzles under the laboratory testing condition of Fan et al. [23]. Concerning the left and right core chambers, the temperature contours of DSC are more symmetric than those of M-DVC. At the middle plane through six nozzles, the temperature contour of DSC through six nozzles is more uniformly distributed than that of M-DVC. It is found that the low temperature plume cannot effectively reach the target wall at the nozzle no.4 of M-DVC which is consistent to its lower  $Nu_{ca}$  peak compared to other nozzles. Moreover, the low temperature plumes of M-DVC are convected slightly downstream which is corresponding to its  $Nu_{ca}$  peak located a little downstream of the center of each nozzle as seen in Fig. 14.

Figure 19 shows the velocity magnitude contours of M-DVC and DSC over the YZ cross section at the middle plane of left and right core chambers and at the middle plane through six nozzles under the laboratory testing condition of Fan et al. [23]. Concerning the left and right core chambers, the velocity magnitude contours of DSC are more symmetric than those of M-DVC. At the middle plane through six nozzles, the velocity magnitude contour of DSC through six nozzles is more uniformly distributed than that of M-DVC. It is found that the impinging jet cannot effectively reach the target wall at the nozzle no.4

of M-DVC which is consistent to its lower  $Nu_{ca}$  peak compared to other nozzles. Moreover, the jet impingement of M-DVC for all six nozzles is weaker than that of DSC which is corresponding to the lower  $Nu_{ca}$  peaks of M-DVC for all nozzles as seen in Fig. 14. At the middle plane through six nozzles, it reveals that DSC induces the stronger axial flow between two nozzles than M-DVC leading to better exhausting heat toward the exit of the core chamber. On the contrary, at the middle plane through six nozzles of M-DVC the cooling air seems to be blocked or stagnant between two nozzles, especially between the nozzle no. 1 & 2, 2 & 3 and 3 & 4, so that it is more difficult for heat to be exhausted toward the exit of the core chamber by the axial flow.

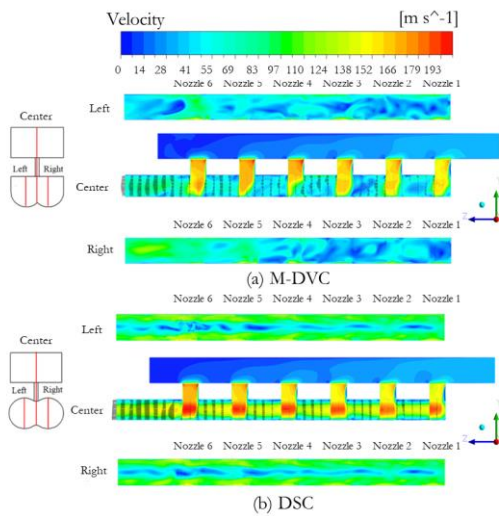


Fig. 19. Velocity magnitude contour over the YZ cross section at the middle plane of left and right core chambers and at the middle plane through six nozzles under the laboratory testing condition of Fan et al. [23]: (a) M-DVC and (b) DSC.

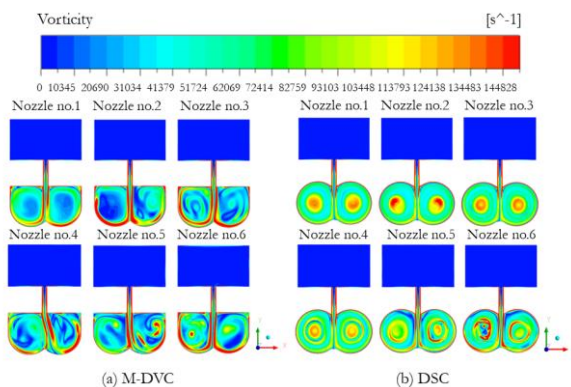


Fig. 20. Vorticity contour over the XY cross section through the middle plane of each individual nozzle under the laboratory testing condition of Fan et al. [23]: (a) M-DVC and (b) DSC.

Figure 20 shows the vorticity contours of M-DVC and DSC over the XY cross section through the middle plane

of each individual nozzle under the laboratory testing condition of Fan et al. [23]. The vorticity of each DSC nozzle is stronger than that of the M-DVC counterpart which can be quantitatively indicated by the cross-sectionally averaged vorticities of DSC and M-DVC as shown in Table 10. The vorticity contour of DSC is more symmetric between left and right core chambers, compared to that of M-DVC.

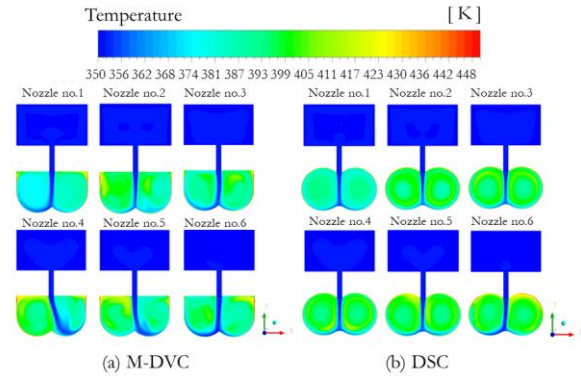


Fig. 21. Temperature contour over the XY cross section through the middle plane of each individual nozzle under the laboratory testing condition of Fan et al. [23]: (a) M-DVC and (b) DSC.

Table 10. Cross-sectionally averaged vorticities of DSC and M-DVC using the laboratory testing condition of Fan et al. [23].

DSC	Left	Right	Cross-sectionally averaged
Nozzle 1	113,788.20	113,716.27	113,752.24
Nozzle 2	112,922.19	112,760.70	112,841.45
Nozzle 3	114,996.00	114,157.08	114,576.54
Nozzle 4	117,668.72	118,007.25	117,837.99
Nozzle 5	111,601.39	118,663.36	115,132.38
Nozzle 6	119,658.19	112,449.96	116,054.08

M-DVC	Left	Right	Cross-sectionally averaged
Nozzle 1	95,831.50	86,276.72	91,054.11
Nozzle 2	84,258.16	95,433.75	90,345.96
Nozzle 3	107,146.44	81,720.57	94,433.50
Nozzle 4	80,181.68	92,994.05	86,587.87
Nozzle 5	80,462.56	93,520.72	86,991.64
Nozzle 6	116,999.90	92,553.57	104,776.73

Figure 21 shows the temperature contours of M-DVC and DSC over the XY cross section through the middle plane of each individual nozzle under the laboratory testing condition of Fan et al. [23]. It is found that the temperature contours of DSC are rather symmetric between left and right core chambers and quite uniform

among six nozzles. On the contrary, symmetry and uniformity are not found in M-DVC

#### 4.2. Comparative Evaluation of DSC and M-DVC under EGAT Real Operating Condition at Base Load

The EGAT real operating condition at base load is conducted at  $Re=40,000$ . Figure 22 shows the distribution of circumferentially averaged Nusselt number along the target wall in the axial direction under the EGAT real operating condition at base load where the simulation result of DSC is compared to the M-DVC one. It is found that all  $Nu_{ca}$  peaks of DSC are higher than the M-DVC ones and the totally averaged Nusselt number of DSC is larger up to 40.07% compared to that of M-DVC as reported in Table 11. The  $Nu_{ca}$  peaks of DSC are more uniform than the M-DVC ones. Two peaks per nozzle of DSC still persist to occur at each nozzle, except the nozzle no.2 and 3 whereas most  $Nu_{ca}$  of M-DVC have one peak, except the nozzle no.1 and 3. It is quite obvious that almost all  $Nu_{ca}$  peaks of M-DVC are convected downstream of the nozzle centers, except at the nozzle no.1 where the nozzle center is approximately located between two  $Nu_{ca}$  peaks. It means that at base load of EGAT real operating condition M-DVC cannot withstand the crossflow effect. For DSC, the  $Nu_{ca}$  peaks of the nozzle no.1-3 are convected downstream of the nozzle centers but for the nozzle no.4-6 the nozzle centers are approximately located inside the valley between two peaks. This implies that DSC is more resistant to the crossflow effect even at real operating condition.

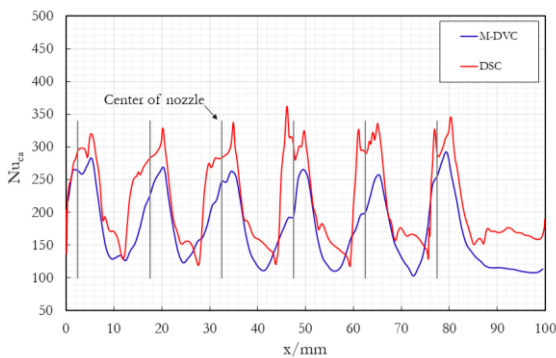


Fig. 22. Circumferentially averaged Nusselt number along the target wall in the axial direction under EGAT real operating condition at base load.

Figure 23 illustrates the Nusselt number contours of M-DVC and DSC on the target wall using the real operating condition of EGAT at base load. It is found that the Nusselt number distribution of DSC is more symmetric to the symmetric line and also more uniform than that of M-DVC. From this contour plot, there seem to be two separate zones of high Nusselt number at each

nozzle, except at the nozzle no.1, for both DSC and M-DVC.

Table 11. Totally averaged Nusselt number, total pressure drop, total pressure drop coefficient and thermal performance factor in case of the real operating condition of EGAT at base load.

Parameter	M-DVC	DSC	Difference (%)
Totally averaged Nusselt number	175.83	246.28	+40.07
Total pressure drop, Pa	63,756.32	61,222.16	-3.97
Total pressure drop coefficient	0.90	0.86	-4.44
Thermal performance factor	0.45	0.64	+42.32

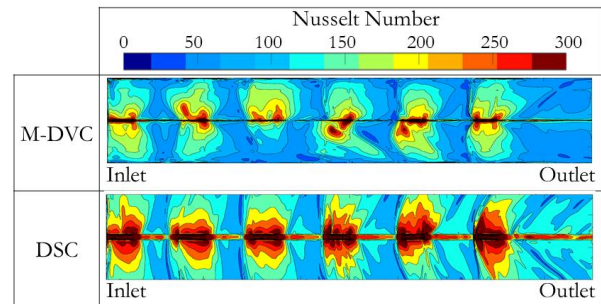


Fig. 23. Nusselt number contours of M-DVC and DSC on the target wall using the real operating condition of EGAT at base load.

In Table 11, the simulation results of the totally averaged Nusselt number, the total pressure drop, the total pressure drop coefficient and the thermal performance factor using the real operating condition of EGAT at base load are summarized in case of DSC and M-DVC. The  $Nu$  of DSC is still higher than that of M-DVC by 40.07% so that DSC can promote better heat transfer than M-DVC even when operated at real operating condition. With real operating condition, the  $Nu$  surplus of DSC over M-DVC drops from 52.64% to 40.07%. The  $\Delta P_T$  and  $\eta$  of DSC are lower than those of M-DVC so that lower friction is encountered when using DSC. The TPF of DSC is still higher than that of M-DVC by 42.32%, even more than when operated in laboratory testing condition, i.e. 38.10% in Table 9.

Figure 24 shows the velocity magnitude contours and streamlines of M-DVC and DSC over the XY cross section through the middle plane of each individual nozzle under the EGAT real operating condition at base load. It is found that the impinging jets of DSC from six nozzles generate the stagnation points at the expecting area as designed which is in the middle between two core

chambers merging to form the target wall opposite to the nozzle exit. For M-DVC, the impinging jets of the nozzle no.2, 3, 4 and 5 miss the target wall and the consequence can be noticed in Fig. 22 where their  $Nu_{ca}$  peaks are lower than those of the nozzle no.1 and 6, meaning lower cooling performance. It also reveals that two counter-rotating vortices formed by DSC are more symmetric for each nozzle and more uniform among six nozzles than those of M-DVC.

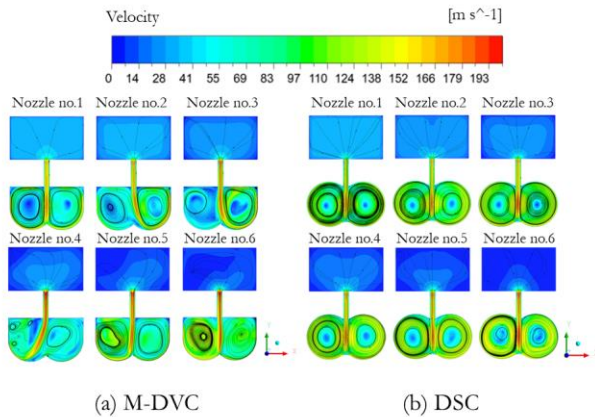


Fig. 24. Velocity magnitude contour and streamline over the XY cross section through the middle plane of each individual nozzle under EGAT real operating condition at base load: (a) M-DVC and (b) DSC.

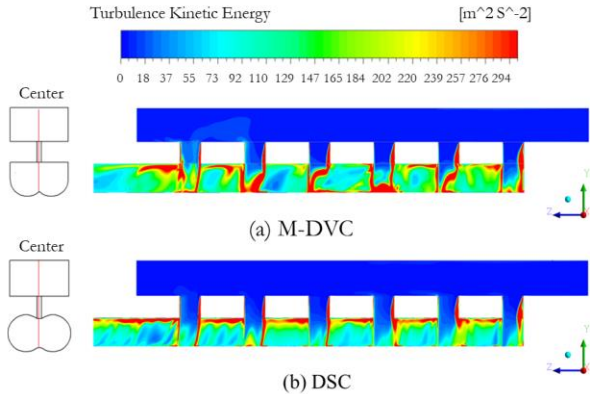


Fig. 25. Turbulence kinetic energy contour over the YZ cross section at the middle plane through six nozzles under EGAT real operating condition at base load: (a) M-DVC and (b) DSC.

Figure 25 displays the turbulence kinetic energy ( $k$ ) contours of M-DVC and DSC over the YZ cross section at the middle plane through six nozzles under the EGAT real operating condition at base load. It reveals that the averaged magnitude of  $k$  over the whole YZ cross section of the core chamber of DSC ( $k_{avg} = 155.89 \text{ m}^2/\text{s}^2$ ) is higher than that of M-DVC ( $k_{avg} = 144.6 \text{ m}^2/\text{s}^2$ ) so that DSC can generate more turbulence to enhance heat transfer. At the nozzle no.2, 3, 4 and 5 of M-DVC, the high- $k$  zones seem not to be pushed down enough toward

the target wall so that their  $Nu_{ca}$  peaks are lower than those of the nozzle no.1 and 6.

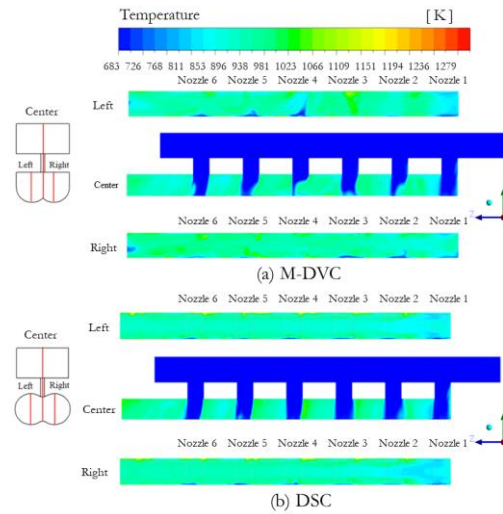


Fig. 26. Temperature contour over the YZ cross section at the middle plane of left and right core chambers and at the middle plane through six nozzles under EGAT real operating condition at base load: (a) M-DVC and (b) DSC.

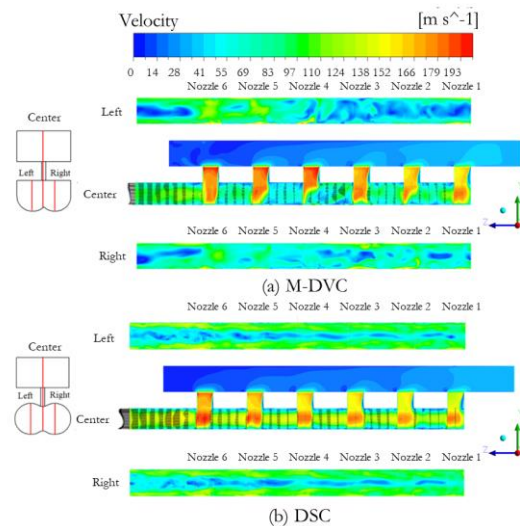


Fig. 27. Velocity magnitude contour over the YZ cross section at the middle plane of left and right core chambers and at the middle plane through six nozzles under EGAT real operating condition at base load: (a) M-DVC and (b) DSC.

Figure 26 illustrates the temperature contours of M-DVC and DSC over the YZ cross section at the middle plane of left and right core chambers and at the middle plane through six nozzles under the EGAT real operating condition at base load. Concerning the left and right core chambers, the temperature contours of DSC are more symmetric than those of M-DVC. At the middle plane through six nozzles, the temperature contour of DSC through six nozzles is more uniformly distributed than that of M-DVC. It is found that the low temperature plumes cannot effectively reach the target wall at the nozzle no.2, 3, 4 and 5 of M-DVC which are consistent to

their lower  $Nu_{ca}$  peaks compared to those of nozzle no.1 and 6. Moreover, the low temperature plumes of M-DVC are convected slightly downstream which is corresponding to its  $Nu_{ca}$  peak located a little downstream of the center of each nozzle as seen in Fig. 22.

Figure 27 shows the velocity magnitude contours of M-DVC and DSC over the YZ cross section at the middle plane of left and right core chambers and at the middle plane through six nozzles under the EGAT real operating condition at base load. Concerning the left and right core chambers, the velocity magnitude contours of DSC are more symmetric than those of M-DVC. At the middle plane through six nozzles, the velocity magnitude contour of DSC through six nozzles is more uniformly distributed than that of M-DVC. It is found that the impinging jets cannot effectively reach the target wall at the nozzle no.2, 3, 4 and 5 of M-DVC which are consistent to their lower  $Nu_{ca}$  peaks compared to those of the nozzle no.1 and 6. Moreover, the jet impingement of M-DVC for all six nozzles is weaker than that of DSC which is corresponding to the lower  $Nu_{ca}$  peaks of M-DVC for all nozzles as seen in Fig. 22. At the middle plane through six nozzles, it reveals that DSC induces the stronger axial flow between two nozzles than M-DVC leading to better exhausting heat toward the exit of the core chamber. On the contrary, at the middle plane through six nozzles of M-DVC the cooling air seems to be blocked/stagnant between two nozzles, especially between the nozzle no.3 & 4 and 4 & 5, so that it is more difficult for heat to be exhausted toward the exit of the core chamber by the axial flow.

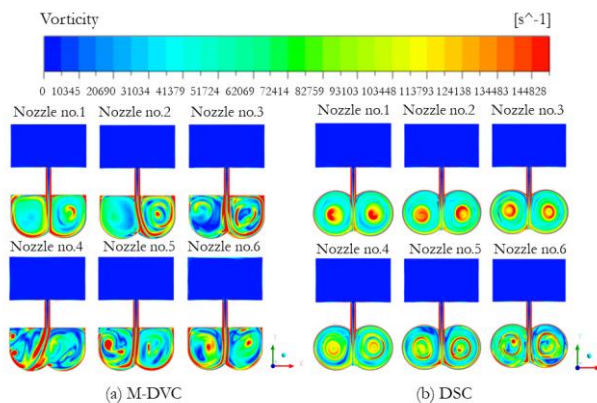


Fig. 28 Vorticity contour over the XY cross section through the middle plane of each individual nozzle under EGAT real operating condition at base load: (a) M-DVC and (b) DSC.

Figure 28 shows the vorticity contours of M-DVC and DSC over the XY cross section through the middle plane of each individual nozzle under the EGAT real operating condition at base load. The vorticity of each DSC nozzle is stronger than that of the M-DVC counterpart, except at the nozzle no.1, which can be quantitatively indicated by

the cross-sectionally averaged vorticity of DSC and M-DVC as shown in Table 12. The vorticity contour of DSC is more symmetric between left and right core chambers, compared to that of M-DVC.

Table 12. Cross-sectionally averaged vorticities of DSC and M-DVC under EGAT real operating condition at base load.

DSC	Left	Right	Cross-sectionally averaged
Nozzle 1	109,466.33	109,928.06	109,697.20
Nozzle 2	110,986.65	110,508.30	110,747.48
Nozzle 3	112,772.74	114,032.67	113,402.71
Nozzle 4	113,170.07	118,785.50	115,977.79
Nozzle 5	106,343.53	117,183.92	111,763.73
Nozzle 6	121,867.08	109,868.34	115,867.71
M-DVC	Left	Right	Cross-sectionally averaged
Nozzle 1	115,438.00	111,995.33	113,716.67
Nozzle 2	85,549.83	124,934.80	105,242.31
Nozzle 3	68,383.85	126,982.16	97,683.00
Nozzle 4	106,369.29	75,272.41	90,820.85
Nozzle 5	113,583.09	103,113.22	108,348.16
Nozzle 6	121,007.14	102,684.46	111,845.80

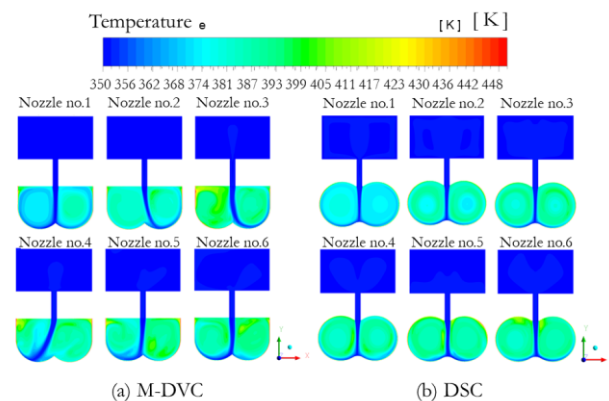


Fig. 29. Temperature contour over the XY cross section through the middle plane of each individual nozzle under EGAT real operating condition at base load: (a) M-DVC and (b) DSC.

Figure 29 shows the temperature contours of M-DVC and DSC over the XY cross section through the middle plane of each individual nozzle under the EGAT real operating condition at base load. It is found that the temperature contours of DSC are rather symmetric between left and right core chambers and quite uniform among six nozzles. On the contrary, symmetry and uniformity are not found in M-DVC.

## 5. Conclusions

Two double swirl/vortex chamber configurations (DSC of Lin et al. [17] and M-DVC of Fan et al. [23]) are numerically investigated by using the RNG  $k-\varepsilon$  turbulence model with enhanced wall treatment which proves to be the most accurate turbulence model for impinging and vortex flows due to its lowest averaged second norms compared to other four turbulence models considered. The cooling performance of DSC and M-DVC is comparatively evaluated under both the laboratory testing condition of Fan et al. [23] and the real operating condition of EGAT at base load. The DSC cooling performance is found to be more effective and efficient because the thermal performance factor of DSC is higher than that of M-DVC for the laboratory testing condition up to 38% and for the real operating condition up to 42%.

## Acknowledgement

Pipat Tansakul is grateful for the tuition-fee-waiving scholarship from TGGS, KMUTNB, during his doctoral study. Phongsakorn Thawornsathit is grateful for the research assistant scholarship from Faculty of Engineering, Kasetsart University, during his Master-Degree study. Both the EGAT and WATA@KU high-performance-computing power is greatly appreciated.

## References

- [1] W. M. Kays and M. E. Crawford, *Convective Heat and Mass Transfer*, 3<sup>rd</sup> ed. McGraw-Hill, 1993.
- [2] J. C. Han, "Recent studies in turbine blade cooling," *Int. J. Rotating Mach.*, vol. 10, no. 6, pp. 443–457, 2004.
- [3] J. C. Han, "Fundamental gas turbine heat transfer," *ASME J. Thermal Sci. Eng. Appl.*, vol. 5 no. 2, 2013.
- [4] J. C. Han, "Advanced cooling in gas turbines 2016 Max Jakob Memorial Award Paper," *ASME J. Heat Trans.*, vol. 140, no. 11, 2018.
- [5] J. Town, D. Straub, J. Black, K.A. Thole, and T. I-P. Shih, "State-of-the-art cooling technology for a turbine rotor blade," *ASME J. Turbomachinery*, vol. 140, no. 7, 2018.
- [6] M. E. Taslim, L. Setayeshgar, and S. D. Spring, "An experimental evaluation of advanced leading edge impingement cooling concepts," *ASME J. Turbomachinery*, vol. 123, no. 1, pp.147-153, 2000.
- [7] M. E. Taslim and D. Bethka, "Experimental and numerical impingement heat transfer in an airfoil leading-edge cooling channel with cross-flow," *ASME J. Turbomachinery*, vol. 131, no. 1, 2008.
- [8] K. Elebiary and M. E. Taslim, "Experimental / numerical crossover jet impingement in an airfoil leading-edge cooling channel," *ASME J. Turbomachinery*, vol. 135, no. 1, 2012.
- [9] L. Yang, J. Ren, H. Jiang, and P. Ligrani, "Experimental and numerical investigation of unsteady impingement cooling within a blade leading edge passage," *Int. J. Heat and Mass Transf.*, vol. 71, pp. 57-68, 2014.
- [10] R. E. Chupp, H. E. Helms, P. W. McFadden, and T. R. Brown, "Evaluation of internal heat transfer coefficient for impingement cooled turbine airfoils," *AIAA J. Aircr.*, vol. 6, pp. 203-208, 1969.
- [11] N. Wang, A. F. Chen, M. Zhang, and J. C. Han, "Turbine blade leading edge cooling with one row of normal or tangential impinging jets," *ASME J. Heat Transfer*, vol. 140, no. 6, 2018.
- [12] Z. Liu, J. Li, and Z. Feng, "Numerical study of swirl cooling in a turbine blade leading-edge model," *J Thermophys. Heat Trans.*, vol. 29, no. 1, pp. 166-178, 2015.
- [13] C. Du, L. Li, X. Wu, and Z. Feng, "Effect of jet nozzle geometry on flow and heat transfer performance of vortex cooling for gas turbine blade leading edge," *Applied Thermal Engineering.*, vol. 93, pp. 1020-1032, 2016.
- [14] X. Fan, L. Li, J. Zou, J. Wang, and F. Wu, "Local heat transfer of vortex cooling with multiple tangential nozzles in a gas turbine blade leading edge cooling passage," *Int. J. Heat Mass Transf.*, vol. 126, pp. 377-389, 2018.
- [15] J. Wang, C. Du, F. Wu, L. Li, and X. Fan, "Investigation of the vortex cooling flow and heat transfer behavior in variable cross-section vortex chambers for gas turbine blade leading edge," *Int. Comm. In Heat Mass Transf.*, vol. 108, 2019.
- [16] N. Wang and J. C. Han, "Swirl impinging cooling on an airfoil leading edge model at large Reynolds number," *ASME J. Thermal Sci. Eng. Appl.*, vol. 11, no. 3, 2019.
- [17] G. Lin, K. Kusterer, A. H. Ayed, D. Bohn, et al., "Numerical investigation on heat transfer in an advanced new leading edge impingement cooling configuration," *Propulsion and Power Research.*, vol. 4, no. 4, pp. 179-189, 2015.
- [18] L. Yang, J. Ren, and H. Jiang, "Experiment and numerical investigation of impingement cooling with spent flow in the blade leading edge," *ISJPPE-2012-A0127*, 2012.
- [19] J. Zhou, X. Wang, J. Li, and W. Hou, "Effects of target channel shapes on double swirl cooling performance at gas turbine blade leading edge," *ASME J. Eng. Gas Turb. Power.*, vol. 141, no. 7, 2019.
- [20] S. Fechter, A. Terzis, P. Ott, B. Weigand, J.V. Wolfersdorf, and M. Cochet, "Experimental and numerical investigation of narrow impingement cooling channels," *Int. J. Heat Mass Transf.*, vol. 67, pp. 1208–1219, 2013.
- [21] G. Lin, K. Kusterer, D. Bohn, et al., "Investigation on heat transfer enhancement and pressure loss of double swirl chambers cooling," *Propulsion and Power Research*, vol. 2, no. 3, pp. 177-187, 2013.
- [22] N. Hay and P. West, "Heat transfer in free swirling flow in a pipe," *J. Heat Transfer*, vol. 97, no. 3, pp. 411–416, 1975.

[23] X. Fan, L. Li, J. Zou, and Y. Zhou, "Cooling methods for gas turbine blade leading edge: comparative study on impingement cooling, vortex

cooling and double vortex cooling," *Int. Comm. In Heat Mass Transf.*, vol. 100, pp. 133-145, 2019.



**Pipat Tansakul** received Bachelor and Master degrees in mechanical engineering from King Mongkut's University of Technology Thonburi (KMUTT), Thailand, in 1997 and 2000 respectively. He has been a Ph.D. candidate in Mechanical Engineering Simulation and Design (MESD) group of The Sirindhorn International Thai-German Graduate School of Engineering (TGGS), King Mongkut's University of Technology North Bangkok (KMUTNB), Thailand, since 2016. He receives the tuition-fee-waving scholarship of TGGS, KMUTNB, during his doctoral study. He is currently Head of Domestic Operation and Maintenance Business Department in Business Management Division at Electricity Generating Authority of Thailand (EGAT). His research interests focus on turbomachinery flow in power plants and gas turbine blade cooling system.



**Thanabodee Sinpo** received B.Eng. degree in materials handling engineering from King Mongkut's University of Technology North Bangkok (KMUTNB), Thailand, in 2016. He has been a Master-Degree student in mechanical engineering simulation and design (MESD) of The Sirindhorn International Thai-German Graduate School of Engineering (TGGS), King Mongkut's University of Technology North Bangkok (KMUTNB), Thailand, since 2017. He receives the tuition-fee-waving scholarship from the Electricity Generating Authority of Thailand (EGAT) project, during his master study. His research interests are turbomachinery flow in power plants and internal cooling for gas turbine blades.



**Phongsakorn Thawornsathit** received B.Eng. degree in mechanical engineering from Kasetsart University Sriracha Campus (KU SRC), Thailand, in 2014. He started working as Building Information Modeling (BIM) engineer at Jardine Engineering Corporation (JEC), Bangkok, Thailand, in 2014. In 2015, he was an inspection engineer at PTT Maintenance and Engineering (PTTME), Rayong, Thailand. In 2017, he pursued M.Eng. degree in mechanical engineering at Kasetsart University (KU), Thailand. During his Master degree, he receives the research assistant scholarship from Faculty of Engineering, KU. Since 2019, he has been a PhD candidate in Mechanical Engineering Simulation and Design (MESD) group at The Sirindhorn International Thai-German Graduate School of Technology (TGGS), King Mongkut's University of Technology North Bangkok (KMUTNB), Thailand. He receives the Thailand Graduate Institute of Science and Technology (TGIST) scholarship of National Science and Technology Development Agency (NSTDA), during his doctoral study. His research interests are MEMS piezoresistive pressure sensor, transition and turbulence modelling and turbomachinery flow in power plants.



**Varangrat Juntasaro** received B.Eng. and Ph.D. degrees in mechanical engineering from Imperial College London, U.K., in 1995 and 1999 respectively with the Royal Thai Government Scholarship. In 1999, she started working as Lecturer at Department of Mechanical Engineering, Faculty of Engineering, Kasetsart University, Bangkok, Thailand, where she became Assistant Professor and Associate Professor in 2001 and 2006 respectively. Her research interests are computational fluid dynamics (CFD), turbulence modelling, and turbomachinery flow in power plants.



**Ekachai Juntasaro** received B.Eng. degree in mechanical engineering from King Mongkut's Institute of Technology Ladkrabang (KMUTT), Thailand, in 1989, and pursued both M.Sc. and Ph.D. degrees in mechanical engineering at Imperial College London, U.K., in 1992 and 1997 respectively with the Royal Thai Government Scholarship. In 1997, he started working as Lecturer at School of Mechanical Engineering, Institute of Engineering, Suranaree University of Technology (SUT), Nakhon Ratchasima, Thailand, where he became Assistant Professor and Associate Professor in 2001 and 2006 respectively. Since 2008, he has worked as Associate Professor in Mechanical Engineering Simulation and Design (MESD) Group at The Sirindhorn International Thai-German Graduate School of Technology (TGGS), King Mongkut's University of Technology North Bangkok (KMUTNB), Thailand. His research interests are transition and turbulence modelling with/without analytical wall function (AWF), unstructured finite volume method for computational fluid dynamics (CFD), microfluidics, and turbomachinery flow in power plants.